Torque Production in Triply-Excited Magnetic Gears

Sri Vignesh Sankarraman
Electrical and Computer Engineering
The University of Texas at Dallas
Dallas, USA
srivignesh.sankarraman@utdallas.edu

Ahmad Daniar
Electrical and Computer Engineering
The University of Texas at Dallas
Dallas, USA
ahmad.daniar@utdallas.edu

Matthew Gardner
Electrical and Computer Engineering
The University of Texas at Dallas
Dallas, USA
matthew.gardner@utdallas.edu

***Abstract*—Magnetic gears (MG) are an important development to improve on the disadvantages of their mechanical counterparts. MGs have multiple topologies with each finding their suitable application. The triply excited magnetic gear (TEMG) is one such topology with interesting possibilities. This topology has an extra set of permanent magnets (PMs) in between the ferromagnetic modulators in addition to the PMs located in the inner and outer rotor. The TEMG topology has multiple variations with respect to PM placements; the torque production in three such variations is studied and compared with the conventional coaxial MG (CCMG). Different geometric parameters are varied and the various topologies are optimized for maximum volumetric torque density (VTD) and permanent magnet specific torque (PM ST). The torque generated by these optimized models is compared, using the finite-element method (FEM), to verify the advantages and disadvantages of the TEMG topologies. The torque production due to the PMs located in between the modulators is minimal compared to the torque produced due to the PMs present in the other two rotors. Thus, the CCMG generally outperforms the TEMG topologies.**

***Index Terms*—coaxial magnetic gear, triply excited magnetic gear, modulators, permanent magnets, volumetric torque density**

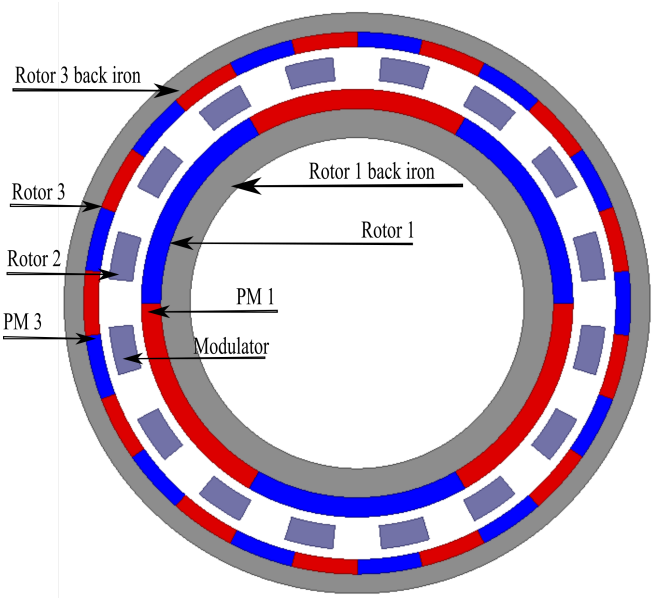

Fig. 1. Conventional coaxial gear (Air gap is exaggerated)

I. Introduction

Mechanical gears have been an integral part of transmission systems for centuries; however, they face mechanical wear and tear, which reduces their reliability. Magnetic gears (MGs) avoid the pitfalls of mechanical gears by removing the physical contact between the teeth and thereby converting low-speed, high-torque rotation to high-speed, low-torque rotation or vice versa more efficiently [1]. Thus, maintenance requirements may be greatly reduced. With the advent of rare earth permanent magnets, the torque density of MGs has increased drastically [2], [3], leading to a recent surge in interest. Due to their potential reliability benefits [4], [5], MGs are being widely studied for aerospace applications [6]–[9], traction and propulsion applications [10]–[12], and wave [13]–[15]and wind energy applications [16], [17].

Like mechanical gears, there are many topologies of MGs that have different advantages suitable for different applications [18], [19]. The radial flux conventional coaxial magnetic gear (CCMG), which is illustrated in Fig. 1, has received the most attention due to the fact that it shows great prospects for high torque densities [20], [2], [4]. In the CCMG, there are three rotors, Rotor 1, Rotor 2, and Rotor 3. Rotor 1 and Rotor 3 have permanent magnets (PMs). Rotor 2 has ferromagnetic modulators, which modulate the flux from the PMs.

The coaxial gear operates using different numbers of pole pairs in Rotor 1 (P_1) and Rotor 3 (P_3). The modulator produces the spatial flux harmonics from the magnetic fields produced from the other two rotors. The spatial flux harmonics interact with each other to produce the gearing action. The magnetomotive forces (MMFs) generated by the PMs in Rotor 1 and Rotor 3 are given by (1) and (2) [21], [22], where F_1 and F_3 are the MMFs generated by the PMs in Rotor 1 and Rotor 3, respectively, $F_{1,m}$ and $F_{3,m}$ are the Fourier series magnitudes, ω_1 and ω_3 are the angular velocities of Rotors 1 and 3, respectively, θ is the angular position in the air gap, and ϕ_1 and ϕ_3 are the initial angular positions of Rotors 1 and 3, respectively.

$$F_1(\theta) = \sum_{m=1,2,3,\ldots}^{\infty} F_{1,m} \cos(mP_1(\theta - \omega_1 t - \phi_1)) \quad (1)$$

$$F_3(\theta) = \sum_{n=1,2,3,\ldots}^{\infty} F_{3,n} \cos(nP_3(\theta - \omega_3 t - \phi_3)) \quad (2)$$

Eqn. (3) gives the permeance function of the modulators in Rotor 2, where Γ_0 is the average value, Γ_k is the permeance harmonic component, Q_2 is the number of modulator pieces in Rotor 2, ω_2 is the angular velocity of Rotor 2 and ϕ_2 is the initial angular position of Rotor 2 [21].

$$\Gamma_2(\theta) = \Gamma_0 + \sum_{k=1,2,3,\ldots}^{\infty} \Gamma_k \cos(kQ_2(\theta - \omega_2 - \phi_2)) \tag{3}$$

The product of the permenance function and the MMF function gives the spatial flux distribution. The spatial flux distributions for Rotor 1 and Rotor 3 are given in (4) and (5), respectively [21].

$$\begin{aligned}\Phi_1(\theta) = &\sum_{m=1,2,3,\ldots}^{\infty} F_{1,m}\Gamma_0 \cos(mP_1(\theta - \omega_1 t - \phi_1)) \\ &+ \sum_{m=1,2,3,\ldots}^{\infty} \sum_{k=1,2,3,\ldots}^{\infty} (\frac{F_{1,m}\Gamma_k}{2}) \cos((mP_1 \pm kQ_2) \\ &(\theta - (\frac{mP_1\omega_1 \pm kQ_2\omega_2}{mP_1 \pm kQ_2})t - (\frac{mP_1\phi_1 \pm kQ_2\phi_2}{mP_1 \pm kQ_2})))\end{aligned} \tag{4}$$

$$\begin{aligned}\Phi_3(\theta) = &\sum_{n=1,2,3,\ldots}^{\infty} F_{3,n}\Gamma_0 \cos(nP_3(\theta - \omega_3 t - \phi_3)) \\ &+ \sum_{n=1,2,3,\ldots}^{\infty} \sum_{k=1,2,3,\ldots}^{\infty} (\frac{F_{3,n}\Gamma_k}{2}) \cos((nP_3 \pm kQ_2) \\ &(\theta - (\frac{nP_3\omega_3 \pm kQ_2\omega_2}{nP_3 \pm kQ_2})t - (\frac{nP_3\phi_3 \pm kQ_2\phi_3}{nP_3 \pm kQ_2})))\end{aligned} \tag{5}$$

The gearing action is achieved by matching the speed and harmonic number of a harmonic from (4) with a harmonic from (5). When *m* is 1 and *k* is 0 in (4) and *n* is 1 and *k* is -1 in (5), (6) gives the relationship between the pole pair counts and the modulator count to match the harmonic numbers [2]. The $-$ sign is not used in (6) because the modulators should not be tangentially wider than the PMs to avoid excessive flux leakage [23]. With the $+$ sign in (6), (7) gives the gear ratio with Rotor 3 fixed [23], [24]. This relationship causes the *m* = 1 and *k* = 0 harmonic in (4) and *n* = 1 and *k* = -1 harmonic in (5) to travel at the same speeds.

$$P_1 \pm P_3 = Q_2 \tag{6}$$

$$G_r = \frac{\omega_1}{\omega_2} = \frac{Q_2}{P_1} \tag{7}$$

To illustrate these harmonics, finite element analysis (FEA) is used to evaluate the radial flux density in the air gaps for the design in Fig. 1, which has P_1 = 3, Q_2 = 16, and P_3 = 13. All analyses were made using Ansys Maxwell 2D magnetostatic simulations. Even though 2D simulations tend to overpredict the torque when compared to 3D simulations [25], the analysis results generally follow the same trends [26]. Figs. 2 and 3 show the harmonic flux densities generated by the PMs in Rotors 1 and 3, respectively, where AG1 is the inner air gap and AG2 is the outer air gap. Fig. 2 shows significant harmonics with spatial frequencies of 3, 9, 13, 15, and 19. The fundamental spatial frequency due to Rotor 1 is 3 (m = 1, k = 0 in (4)). This is modulated to spatial frequencies of 13 (*m* = 1, *k* = -1) and 19 (*m* = 1, *k* = 1). Additionally, odd harmonics of the fundamental are 9 (*m* = 3, *k* = 0) and 15 (*m* = 5, *k* = 0). Similarly, the spatial frequencies of Φ_3 can be obtained from (5) and include 3 (*n* = 1, *k* = -1), 13 (*n* = 1, *k* = 0), and 19 (*n* = 1, *k* = -2). The triply excited magnetic gear (TEMG) topology has been proposed in [27] and [28], which claimed that it achieved better torque density than the CCMG. However, [27] and [28] fail to describe the operating principle by which the TEMG is able to produce extra torque. Additionally, the comparisons made in [27] and [28] are between non-optimized designs. This paper evaluates the different TEMG topologies in [27] and [28]. Section 2 explains the torque generation principle. Section 3 describes the parametric sweep comparison between the topologies. Section 4 provides the results and an analysis of the torque contribution of the different PMs in each topology.

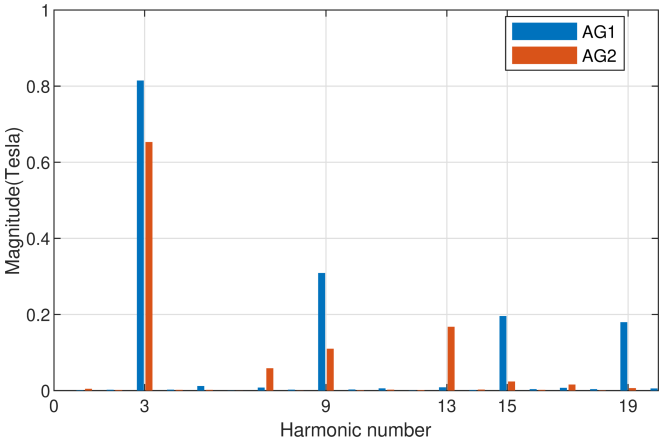

Fig. 2. Harmonic analysis of flux density generated by Rotor 1 PMs in the absence of Rotor 3 PMs (CCMG)

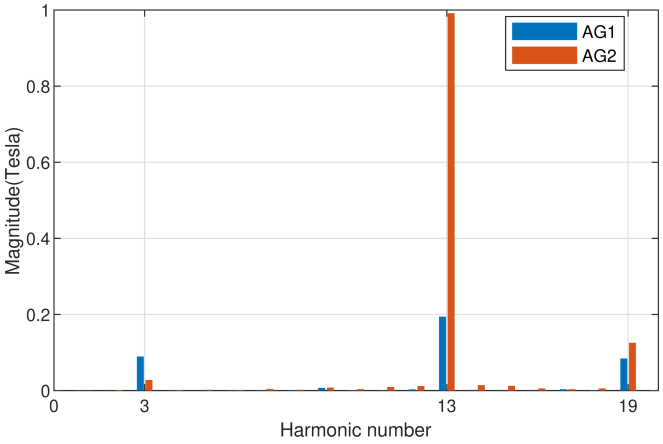

Fig. 3. Harmonic analysis of flux density generated by Rotor 3 PMs in the absence of Rotor 1 PMs (CCMG)

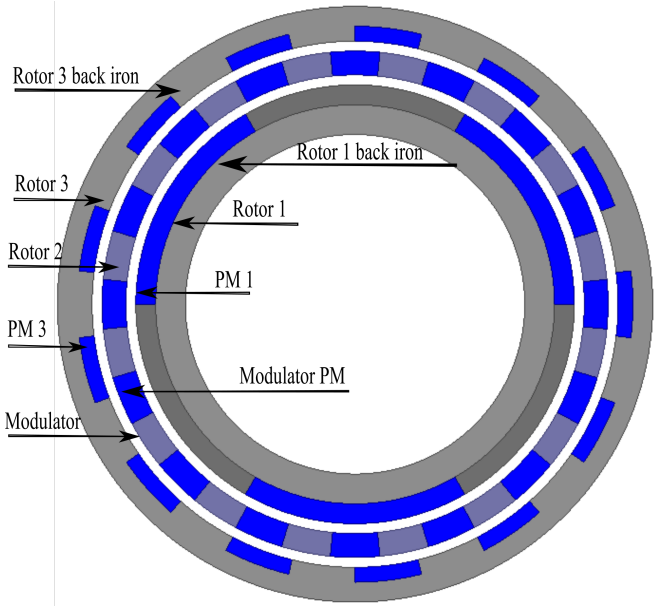

Fig. 4. TEMG Model 1 (Air gap is exaggerated)

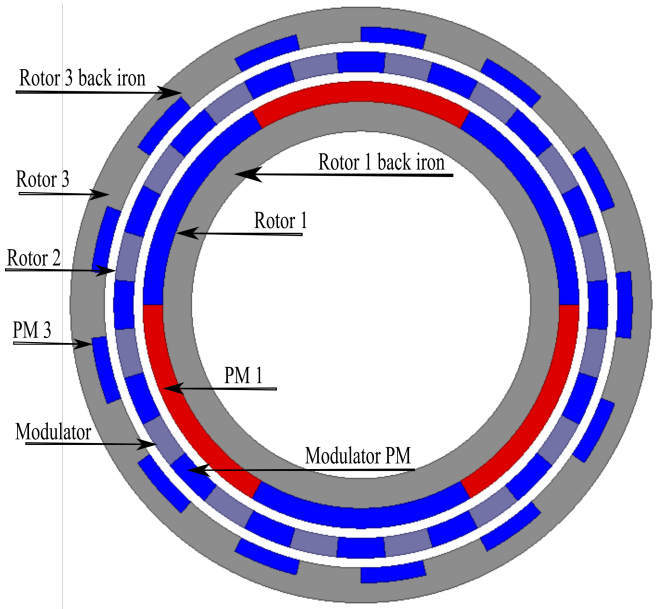

Fig. 5. TEMG Model 2 (Air gap is exaggerated)

II. Torque Generation in TEMG

There are a few variations of TEMG topologies (Figs. 4 - 6), which differ from the CCMG in two major ways. First, PMs are placed between the modulators of Rotor 2. Second, the surface permanent magnet arrangement is replaced with a consequent pole arrangement on Rotor 1 (Fig. 6) or Rotor 3 (Fig. 5) or both (Fig. 4). The ferromagnetic portions of the consequent pole arrangements in Rotors 1 and 3 create permeance functions that modulate the flux from the Rotor 2 PMs. This modulation allows flux harmonics from the Rotor 2 PMs to interact with flux harmonics from the Rotor 1 or Rotor 3 PMs, which can generate additional torque.

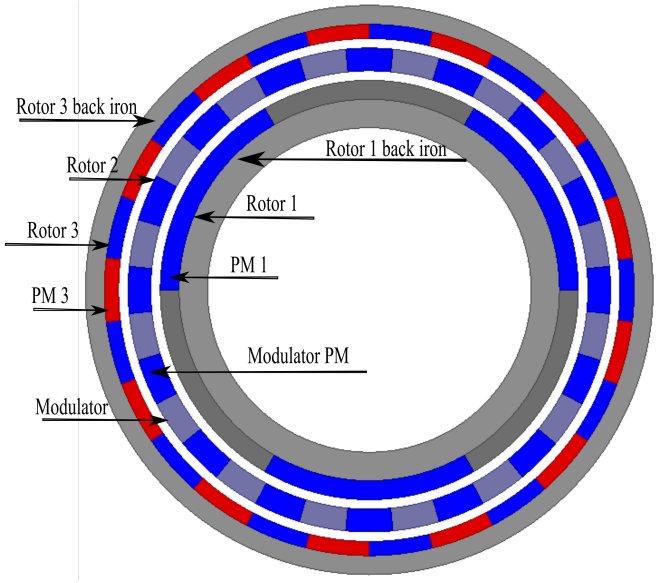

Fig. 6. TEMG Model 3 (Air gap is exaggerated)

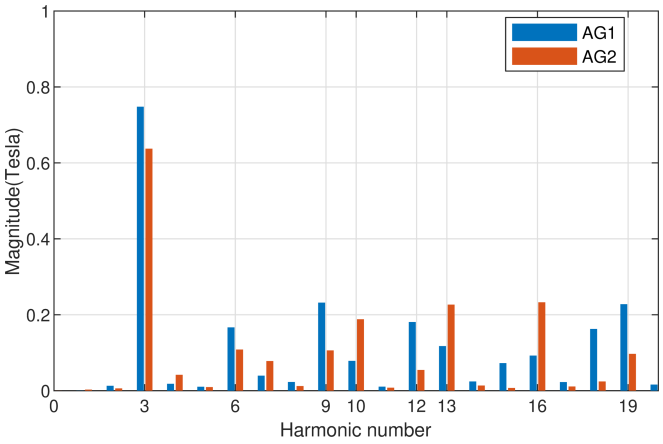

Fig. 7. Harmonic analysis of flux density generated by rotor 1 PMs in the absence of rotor 2 PMs and rotor 3 PMs (TEMG Model 1)

Fig. 4 shows that TEMG Model 1 has consequent pole arrangements in all three rotors. This allows for modulation by the Rotor 1 and Rotor 3 teeth, in addition to the Rotor 2 modulators. This means that there will two new permeance functions similar to (3) but with fundamental spatial frequencies of P_1 and P_3 instead of Q_2. The design shown in Fig. 4 is evaluated using FEA to illustrate the additional spatial harmonics due to the Rotor 2 PMs and the permeance functions from Rotors 1 and 3. This design has $P_1 = 3$, $Q_2 = 16$, and $P_3 = 13$, satisfying (6). The harmonic components of the air gap radial flux density produced by each set of PMs are shown in Figs. 7 - 9.

The Rotor 1 PMs interact with the Rotor 2 modulators and Rotor 3 teeth to produce the harmonics illustrated in Fig. 7.

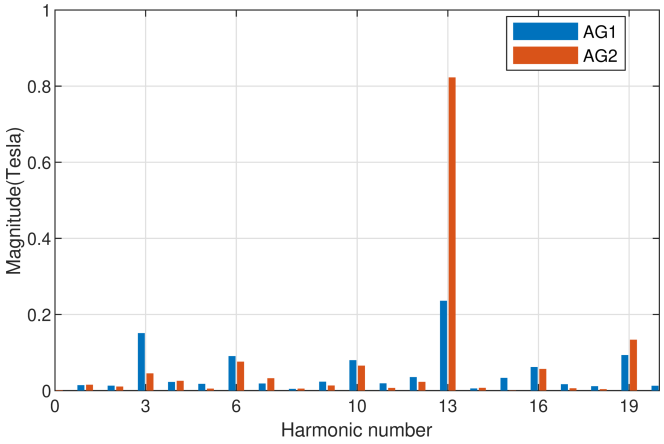

Fig. 8. Harmonic analysis of flux density generated by rotor 3 PMs in the absence of rotor 1 PMs and rotor 2 PMs (TEMG Model 1)

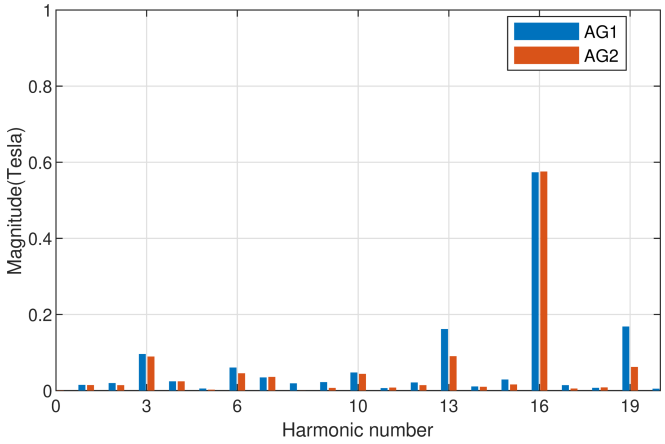

Fig. 9. Harmonic analysis of flux density generated by rotor 2 PMs in the absence of rotor 1 PMs and rotor 3 PMs (TEMG Model 1)

The harmonic components with spatial frequencies of 3, 6, 9, and 12 result from the fundamental MMF produced by the Rotor 1 PMs and its harmonics interacting with the average permeance. Note that unlike the surface permanent magnet arrangement, the consequent pole arrangement can produce even harmonics of the fundamental. The Rotor 1 PMs interact with the 13 Rotor 3 teeth to generate spatial frequencies of 10 and 16. The harmonic with the spatial frequency of 16 will interact with the fundamental of Rotor 2 to produce torque. The Rotor 1 PMs interact with the 16 Rotor 2 modulators to generate spatial frequencies of 13 and 19. The harmonic with the spatial frequency of 13 will interact with the fundamental of Rotor 3.

The Rotor 3 PMs interact with the Rotor 2 modulators and Rotor 1 teeth to produce the harmonics illustrated in Fig. 8. The Rotor 3 PMs interact with the 3 Rotor 1 teeth to generate spatial frequencies of 10 and 16. The harmonic with the spatial frequency of 16 will interact with the fundamental of Rotor 2 to produce torque. The Rotor 3 PMs interact with the 16 Rotor 2 modulators to generate spatial frequencies of 3 and 29. The harmonic with the spatial frequency of 3 will interact with the fundamental of Rotor 1. The spatial frequencies of 6 and 19 stem from the interaction of the second harmonic components in the MMF or the permeance functions.

The Rotor 2 PMs interact with the Rotor 3 teeth and Rotor 1 teeth to produce the harmonics illustrated in Fig. 9. The Rotor 2 PMs interact with the 3 Rotor 1 teeth to generate spatial frequencies of 13 and 19. The harmonic with the spatial frequency of 13 will interact with the fundamental of Rotor 3 to produce torque. The Rotor 2 PMs also interact with the 13 Rotor 3 teeth to generate spatial frequencies of 3 and 29. The harmonic with the spatial frequency of 3 will interact with the fundamental of Rotor 1.

Even though the Rotor 2 PMs produce harmonics that can generate additional torque, Figs. 7 and 8 show that the magnitudes of the fundamental flux density from Rotor 1 and Rotor 3 PMs are lower than the flux densities obtained from

TABLE I
FUNDAMENTAL FREQUENCIES FOR DIFFERENT TOPOLOGIES

MMF Rotor	Modulating Rotor	Spatial Frequency	CCMG	TEMG Model 1	TEMG Model 2	TEMG Model 3
1	2	Q_2 - P_1 = P_3	X	X	X	X
1	3	P_1 + P_3 = Q_2		X	X	
2	1	Q_2 - P_1 = P_3		X		X
2	3	Q_2 - P_3 = P_1		X	X	
3	1	P_1 + P_3 = Q_2		X		X
3	2	Q_2 - P_3 = P_1	X	X	X	X

the CCMG (Figs. 2 and 3), due to the replacement of the surface permanent magnet arrangement with the consequent pole arrangement. Thus, these additional torque-producing harmonics may come at the cost of reduced torque generation by the main torque-producing harmonics of the CCMG. TEMG Model 2 and TEMG Model 3 are similar to TEMG Model 1 but have a surface permanent magnet arrangement on either Rotor 1 or Rotor 3. Thus, flux can only be modulated by two of the rotors. Table I shows the torque-producing harmonics in each of the models.

III. Parametric Sweep Study

The previous section shows that the TEMG has additional torque producing harmonics, but the air gap flux density magnitude is reduced by the use of consequent pole arrangements on Rotor 1 and Rotor 3. Each topology was parametrically swept over the parameter values shown in Table II to obtain a fair basis of comparison. In Table II, the a:b:c notation indicates that the parameter was swept from a to c in steps of b. Each design case was evaluated using Ansys Maxwell 2D magnetostatic simulations. M19 steel was used for ferromagnetic components, and NdFeB N50H was used for all PMs, which are discrete, radially magnetized, and arc shaped. The operational temperature for the magnets was assumed to be around 20 °C. The goal here is for each model to have maximum volumetric torque density (VTD) and permanent magnet specific torque (PM ST) which are defined in (8) and

TABLE II
PARAMETERS CONSIDERED FOR THE PARAMETRIC SWEEP

Parameter	Description	Value	Unit
P_1	Rotor 1 PM pole pairs	4:2:12	
G_{int}	Integer part of gear ratio	4,8,16	
R_{out}	Outer radius	100	mm
T_{BI1}	Rotor 1 back iron thickness	10	mm
T_{PM1}	Rotor 1 PM thickness	5,7.5,10	mm
T_{Mods}	Rotor 2 thickness	5,7.5,10	mm
T_{AG}	Air gap thickness	1	mm
K_{PM13}	Rotors 3 and 1 PM thickness ratio	0.5,0.75,1	
T_{BI3}	Rotor 3 back iron thickness	10	mm
$Mods_{ff}$	Modulators tangential fill factor	0.4:0.05:0.6	
$PM1_{ff}$	Rotor 1 PMs fill factor	0.4:0.1:0.8	
$PM3_{ff}$	Rotor 3 PMs fill factor	0.4:0.1:0.8	

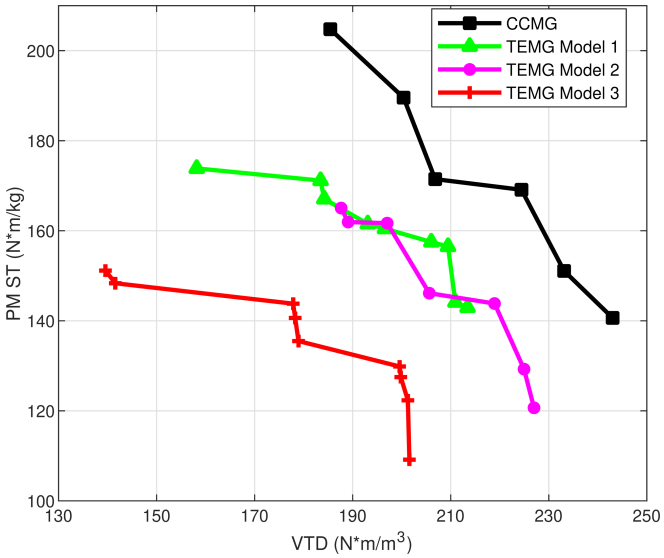

Fig. 10. Pareto front for VTD vs PM ST for G_{int} = 4

(9), respectively [29].

$$\text{VTD} = \frac{\text{Rotor 2 slip torque}}{\text{active volume}} \tag{8}$$

$$\text{PM ST} = \frac{\text{Rotor 2 slip torque}}{\text{total PM mass}} \tag{9}$$

From (10) P_3 is calculated with G_{int} and P_1, where % denotes the modulus operation [24], [26]. This yields a non-integer gear ratio, which reduces the torque ripple relative to an integer gear ratio, and a design with symmetry, which mitigates unbalanced magnetic forces. Eq. (11) defines the Rotor 3 PM thickness (T_{PM3}) in terms of K_{PM13} and T_{PM1} [24], [26]. $PM1_{ff}$ and $PM3_{ff}$ are only applied to rotors with consequent poles, but 100% fill factors are assumed for rotors with surface permanent magnets.

$$P_3 = (P_1(G_{int} - 1)) + 1 + ((P_1 G_{int})\%2) \tag{10}$$

$$T_{PM3} = K_{PM13} T_{PM1} \tag{11}$$

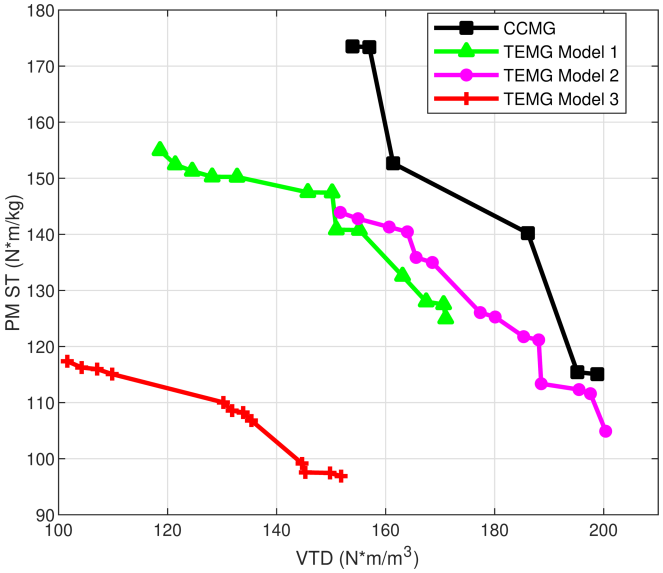

Fig. 11. Pareto front for VTD vs PM ST for G_{int} = 8

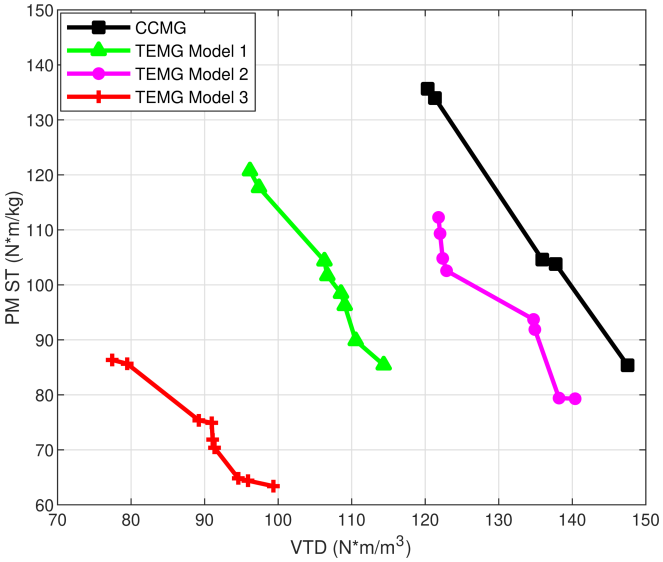

Fig. 12. Pareto front for VTD vs PM ST for G_{int} = 16

IV. QUANTITATIVE TORQUE COMPARISON

All 4 models are simulated with the parameters listed in Table II and the VTD and PM ST are calculated for each design. Using these data the Pareto fronts for the VTD and the PM ST are plotted for each model for each G_{int}. Figs. 10, 11, and 12 show the Pareto fronts for G_{int} values of 4, 8, and 16, respectively.

The extremities of each front provide the maximum VTD and the maximum PM ST. Figs. 10, 11, and 12 show that the CCMG generally outperforms the TEMG models, although when the gear ratio is 8, the maximum VTD generated by TEMG Model 2 is slightly higher than that of the CCMG. Among the TEMG models, TEMG Model 3 provides the

TABLE III
TORQUE DUE TO DIFFERENT PMS FOR MAXIMUM VTD DESIGNS

	All magnets	PM2 & PM3	PM1 & PM2	PM1 & PM3
Gr = 4				
CCMG	764 Nm	N/A	N/A	764 Nm (100%)
TEMG Model 1	635 Nm	57 Nm (9.0%)	215 Nm (33.90%)	488 Nm (76.9%)
TEMG Model 2	684 Nm	0 Nm (0%)	226 Nm (33.0%)	580 Nm (84.80%)
TEMG Model 3	604 Nm	47 Nm (7.80%)	0 Nm (0%)	585 Nm (96.90%)
Gr = 8				
CCMG	616 Nm	N/A	N/A	616 Nm (100%)
TEMG Model 1	527 Nm	32 Nm (6.10%)	256 Nm (48.60%)	363 Nm (68.90%)
TEMG Model 2	598 Nm	0 Nm (0%)	244 Nm (40.80%)	459 Nm (76.80%)
TEMG Model 3	463 Nm	19 Nm (4.10%)	0 Nm (0%)	446 Nm (96.30%)
Gr = 16				
CCMG	448 Nm	N/A	N/A	448 Nm (100%)
TEMG Model 1	367 Nm	1 Nm (0.30%)	191 Nm (52%)	263 Nm (71.70%)
TEMG Model 2	429 Nm	0 Nm (0%)	199 Nm (46.40%)	315 Nm (73.40%)
TEMG Model 3	326 Nm	1 Nm (0.30%)	0 Nm (0%)	324 Nm (99.40%)

TABLE IV
TORQUE DUE TO DIFFERENT PMS FOR MAXIMUM PM ST DESIGNS

	All magnets	PM2 & PM3	PM1 & PM2	PM1 & PM3
Gr = 4				
CCMG	581 Nm	N/A	N/A	581 Nm (100%)
TEMG Model 1	499 Nm	31 Nm (6.2%)	155 Nm (31.1%)	374 Nm (74.9%)
TEMG Model 2	568 Nm	0 Nm (0%)	174 Nm (30.6%)	473 Nm (83.30%)
TEMG Model 3	441 Nm	17 Nm (3.90%)	0 Nm (0%)	432 Nm (98.0%)
Gr = 8				
CCMG	482 Nm	N/A	N/A	482 Nm (100%)
TEMG Model 1	341 Nm	20 Nm (5.90%)	110 Nm (32.30%)	206 Nm (60.40%)
TEMG Model 2	485 Nm	0 Nm (0%)	189 Nm (39.0%)	348 Nm (71.80%)
TEMG Model 3	277 Nm	16 Nm (5.80%)	0 Nm (0%)	267 Nm (96.40%)
Gr = 16				
CCMG	375 Nm	N/A	N/A	375 Nm (100%)
TEMG Model 1	302 Nm	5 Nm (1.70%)	133 Nm (44%)	186 Nm (61.60%)
TEMG Model 2	375 Nm	0 Nm (0%)	175 Nm (46.7%)	257 Nm (68.50%)
TEMG Model 3	234 Nm	3 Nm (1.30%)	0 Nm (0%)	230 Nm (98.30%)

worst performance. Ref. [27] provides anecdotal evidence for TEMG Model 2 providing better performance than the CCMG, which contradicts the trend from the parametric sweep. This discrepancy can be attributed to the [27] comparing non-optimized models.

As these results showing that the CCMG generally outperforms the TEMG models were unexpected, the torque production due to different sets of magnet interaction is evaluated to further understand the torque contribution of the modulator PMs. Two sets of magnets are required to generate torque. By removing one set of PMs from one rotor, the contribution of the remaining set of PMs to the total torque generation can be determined for the TEMG models. Since the CCMG has only two sets of PMs, removing either set of PMs will result in zero torque production. Tables III and IV gives the torque generated by each model at different gear ratios for the maximum VTD and PM ST versions. The stack length of the gear is assumed to be 100 mm. The numbers in parentheses indicate the percentage of the torque relative to when all sets of PMs are present.

For each of the topologies, Tables III and IV show that the interaction producing the largest torque is between the PM1s and PM3s. For the TEMG models, this torque is less than the CCMG because the TEMG models employ consequent pole arrangements on Rotors 1 or 3 to modulate the flux generated by the PM2s. As illustrated in Figs. 2, 3, 7 and 8, replacing surface permanent magnet arrangements with consequent pole arrangements reduces the fundamental flux density magnitudes produced by the PM1s and PM3s in their respective air gaps. Even though the interaction between the PM2s and the other PMs generates additional torque, the total torque generated by the TEMG models is generally less than the CCMG. Due to the high pole count of the PM2s and their small size compared to the other PMs, they produce a considerable amount of leakage flux. This leakage flux does not contribute to torque production but does contribute to saturation. The torque produced by the interaction of the PM3s and the PM2s is particularly small due to their high pole counts, especially at higher gear ratios. Thus, TEMG Model 3 achieves the worst performance.

V. CONCLUSION

The triply excited magnetic gear model does not provide any improvement over the conventional magnetic gear model when the comparison is made based on optimized designs. The key takeaways from this study are as follow:

- The TEMG models generate more flux density harmonics than the CCMG model, as shown in Figs. 2, 3, and 7 - 9.

Some of these harmonics contribute to additional useful torque production, but others may only contribute to torque ripple, saturation, and losses.

- The conventional topology generally provides better results in terms of the VTD and PM ST.
- The modulator permanent magnet's contributions to the torque production are much smaller than the torque produced by the interaction of the PMs present in Rotors 1 and 3.
- For the TEMG topology, at least one of the rotors should have a consequent pole structure to have torque generation; this reduces the torque produced by the interaction of the PMs present in Rotors 1 and 3.
- The consequent pole structure on Rotor 3 is less detrimental than the consequent pole structure on Rotor 1.

Even though the torque generation is better with the consequent pole structure on Rotor 3, using consequent poles on Rotor 1 may provide mechanical advantages in terms of holding the PMs in position during high-speed operation.

REFERENCES

[1] M. C. Gardner, M. Johnson, and H. A. Toliyat, "Analysis of High Gear Ratio Capabilities for Single-Stage, Series Multistage, and Compound Differential Coaxial Magnetic Gears," *IEEE Trans. Energy Convers.*, vol. 34, no. 2, pp. 665–672, 2019.

[2] K. Atallah and D. Howe, "A novel high-performance magnetic gear," *IEEE Trans. Magn.*, vol. 37, no. 4, pp. 2844–2846.

[3] L. Jian and K. T. Chau, "A coaxial magnetic gear with halbach permanent-magnet arrays," *IEEE Trans. Energy Convers.*, vol. 25, no. 2, pp. 319–328, 2010.

[4] P. O. Rasmussen, T. O. Andersen, F. T. Jørgensen, and O. Nielsen, "Development of a high-performance magnetic gear," *IEEE Trans. Ind. Appl.*, vol. 41, no. 3, pp. 764–770, 2005.

[5] E. Gouda, S. Mezani, L. Baghli, and A. Rezzoug, "Comparative study between mechanical and magnetic planetary gears," *IEEE Trans. Magn.*, vol. 47, no. 2, pp. 439–450, 2011.

[6] H. Y. David Wong, H. Baninajar, B. Dechant, and J. Bird, "Designing a Magnetic Gear for an Electric Aircraft Drivetrain," *Proc. IEEE Energy Conver. Congr. Expo*, pp. 6391–6398, 2020.

[7] T. F. Tallerico, Z. A. Cameron, and J. J. Scheidler, "Design of a magnetic gear for nasa's vertical lift quadrotor concept vehicle," *Proc. AIAA Propulsion and Energy Forum*, pp. 1–21, 2019.

[8] T. F. Tallerico, Z. A. Cameron, J. J. Scheidler, and H. Hasseeb, "Outer stator magnetically-geared motors for electrified urban air mobility vehicles," *Proc. AIAA Propulsion and Energy Forum*, pp. 1–25, 2020.

[9] J. Z. Bird, "A Review of Electric Aircraft Drivetrain Motor Technology," *IEEE Trans. Magn.*, vol. 58, no. 2, 2022.

[10] L. Jing, W. Tang, T. Wang, T. Ben, and R. Qu, "Performance Analysis of Magnetically Geared Permanent Magnet Brushless Motor for Hybrid Electric Vehicles," *IEEE Trans. Transport. Electrific.*, vol. 8, no. 2, pp. 2874–2883, 2022.

[11] T. V. Frandsen, L. Mathe, N. I. Berg, R. K. Holm, T. N. Matzen, P. O. Rasmussen, and K. K. Jensen, "Motor Integrated Permanent Magnet Gear in a Battery Electrical Vehicle," *IEEE Trans. Ind. Appl.*, vol. 51, no. 2, pp. 1516–1525, 2015.

[12] K. T. Chau, D. Zhang, J. Z. Jiang, C. Liu, and Y. Zhang, "Design of a magnetic-geared outer-rotor permanent-magnet brushless motor for electric vehicles," *IEEE Trans. Magn.*, vol. 43, no. 6, pp. 2504–2506.

[13] M. Johnson, M. C. Gardner, H. A. Toliyat, S. Englebretson, W. Ouyang, and C. Tschida, "Design, Construction, and Analysis of a Large-Scale Inner Stator Radial Flux Magnetically Geared Generator for Wave Energy Conversion," *IEEE Trans. Ind. Appl.*, vol. 54, no. 4, pp. 3305–3314, 2018.

[14] H. Baninajar, J. Z. Bird, S. Modaresahmadi, and W. Williams, "Electromagnetic and Mechanical Design of a Hermetically Sealed Magnetic Gear for a Marine Hydrokinetic Generator," *Proc. IEEE Energy Conver. Congr. Expo*, pp. 4987–4993, 2018.

[15] W. Li, K. T. Chau, and J. Z. Jiang, "Application of linear magnetic gears for pseudo-direct-drive oceanic wave energy harvesting," *IEEE Trans. Magn*, vol. 47, no. 10, pp. 2624–2627, 2011.

[16] K. Li, S. Modaresahmadi, W. B. Williams, J. Z. Bird, J. D. Wright, and D. Barnett, "Electromagnetic Analysis and Experimental Testing of a Flux Focusing Wind Turbine Magnetic Gearbox," *IEEE Trans. Energy Convers.*, vol. 34, no. 3, pp. 1512–1521, 2019.

[17] L. Jian, K. T. Chau, and J. Z. Jiang, "A magnetic-geared outer-rotor permanent-magnet brushless machine for wind power generation," *IEEE Trans. Ind. Appl.*, vol. 45, no. 3, pp. 954–962, 2009.

[18] Y. Wang, M. Filippini, N. Bianchi, and P. Alotto, "A Review on Magnetic Gears: Topologies, Computational Models, and Design Aspects," *IEEE Trans. Ind. Appl.*, vol. 55, no. 5, pp. 4557–4566, 2019.

[19] P. M. Tlali, R. J. Wang, and S. Gerber, "Magnetic gear technologies: A review," *Proc. Int. Conf. Elect. Mach.*, pp. 544–550, 2014.

[20] H. Y. Wong, J. Z. Bird, D. Barnett, and W. Williams, "A high torque density halbach rotor coaxial magnetic gear," *Proc. IEEE Int. Elect. Mach. & Drives Conf.*, pp. 233–239, 2019.

[21] H. A. Toliyat, M. Johnson, and M. C. Gardner, "Magnetic Gears and Magnetically Geared Machines: An Alternative Compact and Reliable Solution for High-Torque, Low-Speed Systems," pp. 389–420, 2020.

[22] X. Zhang, X. Liu, and Z. Chen, "Investigation of Unbalanced Magnetic Force in Magnetic Geared Machine Using Analytical Methods," *IEEE Trans. Magn*, vol. 52, no. 7, pp. 2–5, 2016.

[23] B. Praslicka, M. C. Gardner, M. Johnson, and H. A. Toliyat, "Review and Analysis of Coaxial Magnetic Gear Pole Pair Count Selection Effects," *IEEE Trans. Emerg. Sel. Topics Power Electron*, vol. 10, no. 2, pp. 1813–1822, 2022.

[24] M. C. Gardner, M. Johnson, and H. A. Toliyat, "Performance Impacts of Practical Fabrication Tradeoffs for a Radial Flux Coaxial Magnetic Gear with Halbach Arrays and Air Cores," *Proc. IEEE Energy Conver. Congr. Expo*, pp. 3129–3136, 2019.

[25] S. Gerber and R. J. Wang, "Analysis of the end-effects in magnetic gears and magnetically geared machines," *Proc. Int. Conf. Elect. Mach.*, pp. 396–402, 2014.

[26] M. C. Gardner, M. Johnson, and H. A. Toliyat, "Comparison of Surface Permanent Magnet Coaxial and Cycloidal Radial Flux Magnetic Gears," *Proc. IEEE Energy Conver. Congr. Expo*, vol. 54, no. 3, pp. 5005–5012, 2018.

[27] S. Peng, W. N. Fu, and S. L. Ho, "A novel high torque-density triple-permanent-magnet-excited magnetic gear," *IEEE Trans. Magn*, vol. 50, no. 11, pp. 11–14, 2014.

[28] Y. Chen, W. N. Fu, and W. Li, "Performance Analysis of a Novel Triple-Permanent-Magnet-Excited Magnetic Gear and Its Design Method," *IEEE Trans. Magn.*, vol. 52, no. 7, pp. 7–10, 2016.

[29] M. C. Gardner, M. Johnson, and H. A. Toliyat, "Comparison of Surface Permanent Magnet Coaxial and Cycloidal Radial Flux Magnetic Gears," *Proc. IEEE Energy Conver. Congr. Expo*, vol. 33, no. 4, pp. 5005–5012, 2018.

Sri Vignesh Sankarraman (S'22) earned his B.E. degree in electrical and electronics engineering from Anna University, India, in 2016, and the M.Sc. degree in electrical power engineering from RWTH Aachen University, Aachen, Germany, in 2019. He is currently working toward his Ph.D. degree in electrical engineering with The University of Texas at Dallas, Richardson, TX, USA. His research interests include design, optimization, and control of electric machines, magnetic gears and power converters.

Ahmad Daniar (S'20) earned his B.Sc. degree in electrical engineering from the University of Tabriz, Tabriz, Iran, in 2014, and the M.Sc. degree in electrical engineering from Sharif University of Technology, Tehran, Iran, in 2017. He is currently working toward his Ph.D. degree in electrical engineering with The University of Texas at Dallas, Richardson, TX, USA. His research interests include design, modelling, optimization, and control of electric machines and power converters.

Matthew C. Gardner (S' 15, M' 19) earned his B.S. in electrical engineering from Baylor University, Waco, Texas in 2014. He earned his Ph.D. in electrical engineering from Texas A&M University, College Station, Texas in 2019. In August 2020, he joined the University of Texas at Dallas, where he is an assistant professor. His research interests include optimal design and control of electric machines and magnetic gears.